(article starts on next page)

Phase stability and structural transitions in compositionally complex LnMO$_3$ perovskites

Johan Cedervall [a,b,*], Rebecca Clulow [c], Hanna L.B. Boström [c,d], Deep C. Joshi [e],
Mikael S. Andersson [e,f], Roland Mathieu [e], Premysl Beran [g,h], Ronald I. Smith [b], Jo-Chi Tseng [i],
Martin Sahlberg [c], Pedro Berastegui [c], Samrand Shafeie [c,j]

[a] Department of Materials and Environmental Chemistry, Stockholm University, SE, 10691, Stockholm, Sweden
[b] ISIS Pulsed Neutron & Muon Facility, Rutherford Appleton Laboratory, Harwell Campus, OX11 0QX, United Kingdom
[c] Department of Chemistry - Ångström Laboratory, Uppsala University, Box 538, 751 21, Uppsala, Sweden
[d] Max Planck Institute for Solid State Research, Heisenbergsstrasse 1, 70569, Stuttgart, Germany
[e] Department of Materials Science and Engineering, Uppsala University, Box 35, 751 03, Uppsala, Sweden
[f] Department of Chemistry and Chemical Engineering, Chalmers University of Technology, Göteborg, 412 96, Sweden
[g] Nuclear Physics Institute, Academy of Sciences of the Czech Republic, 25068, Rez, Czech Republic
[h] European Spallation Source ESS ERIC, Box 176, 221 00, Lund, Sweden
[i] Deutsches Elektronen-Synchrotron (DESY), Notkestraße 85, 22607, Hamburg, Germany
[j] Department of Physics, Chalmers University of Technology, Göteborg, 412 96, Sweden

ARTICLE INFO

ABSTRACT

Entropy stabilised materials have possibilities for tailoring functionalities to overcome challenges in materials science. The concept of configurational entropy can also be applied to metal oxides, but it is unclear whether these could be considered as solid solutions in the case of perovskite-structured oxides and if the configurational entropy plays a stabilising role. In this study, compositionally complex perovskite oxides, LnMO$_3$ (Ln = La, Nd, Sm, Ca and Sr, M = Ti, Cr, Mn, Fe, Co, Ni, and Cu), are investigated for their phase stability and magnetic behaviour. Phase-pure samples were synthesised, and the room temperature structures were found to crystallise in either *Pnma* or *R$\overline{3}$c* space groups, depending on the composition and the resulting tolerance factor, while the structural transition temperatures correlate with the pseudo cubic unit cell volume. The techniques used included diffraction with X-rays and neutrons, both *ex-* and *in-situ*, X-ray photoelectron spectroscopy, magnetometry as well as electron microscopy. Neutron diffraction studies on one sample reveal that no oxygen vacancies are found in the structure and that the magnetic properties are ferrimagnetic-like with magnetic moments mainly coupled antiferromagnetically along the crystallographic *c*-direction. X-ray photoelectron spectroscopy gave indications of the oxidation states of the constituting ions where several mixed oxidation states are observed in these valence-compensated perovskites.

1. Introduction

Perovskite oxides (ABO$_3$) are a class of materials with interesting electronic, magnetic and transport properties of technological relevance [1–4]. These materials display a versatile functionality that can in part be attributed to the vast scope for compositional variation, as nearly any cation in the periodic table can be incorporated in the perovskite structure. Commonly, the A-site contains a large cation *e.g.*, a lanthanide (Ln), or a group I or II cation. The B-site contains mainly smaller cations from the 3d, 4d, and 5d elements, but other cations from the semi-metals and

non-metals can also be included. The crystal structure therefore provides a nearly endless compositional degree of freedom for the modification and optimization of the properties.

Introducing chemical disorder in the structure by means of partial substitutions significantly influences the physical properties. For example, in LaMnO$_3$, A-site doping results in the mixed-valent manganites that exhibit giant magnetoresistance [5–7], where the thermal transport properties are also influenced by local distortions of the MnO$_6$ octahedra [8]. Moreover, an inhomogeneous distribution of two or more cations on the B-site is integral for relaxor ferroelectrics and ferromagnets

---

[9–11]. Generally, the subject of most studies has been the effect of compositional variation on the properties with only two cations on either the A- or the B-site. However, compositionally complex oxides with up to six cations on each site have recently been reported in the literature [12–14]. These new systems broaden the scope for configurational disorder and are closely linked to the concept of high-entropy alloys.

Apart from the widespread use of the high entropy approach in metal alloys, the concept of increasing configurational entropy has recently also been utilised in other systems such as carbides, borides, and oxides [14–18]. MO-type oxides with five cations have been reported to comply with the definition of an oxide with a dominating entropy part which induces a reversible phase transition between a single phase at high temperature and several MO-type phases at lower temperatures [17]. In this case of "high entropy oxides" (HEO), the transition temperature also decreases with an increasing number of elements, as predicted from the increased entropy contribution to the Gibbs free energy. However, this effect remains to be confirmed in other compositionally complex oxide systems raising the question if these are also to be considered entropy-stabilised oxides [19].

In addition to the rock-salt MO-type oxide mentioned above, the perovskite structure can also accommodate a large number of cations. For perovskite-based materials, the stability of the structure is governed by the relative sizes of the atoms involved. This can be quantified using the Goldschmidt tolerance factor as shown in Equation (1), where t, R_A, R_B and R_O are the tolerance factor, A-cation radius, B-cation radius and O-anion radius respectively.

$$t = \frac{R_A + R_O}{\sqrt{2}(R_B + R_O)} \qquad (1)$$

For an ideal cubic perovskite, *t* should be close to 1, whereas at $t > 1$, the hexagonal perovskite-type structures are stabilised. At $t < 1$ the structure may transition through trigonal, tetragonal, orthorhombic and monoclinic symmetry as *t* decreases [20]. Additionally, the average symmetry is determined by the ordering of the cations. The introduction of additional degrees of freedom from configurational entropy, namely by multi atom substitution at the A and B-sites of the perovskite, could lead to improved compositional control. This in turn could lead to a higher degree of tunability of both the physical and structural properties of the materials. The stability as single phase materials of compositionally complex perovskites cannot be easily described with parameters like the tolerance factor or the entropy of mixing. There is a need to understand the contribution of configurational entropy, phase changes and the effect of constituent cations [21].

The physical properties of several high entropy ceramics have recently been reviewed, revealing improvements over simpler compounds for numerous applications, including low thermal conductivity, ion transport and catalytic properties [22,23]. However, the properties of high entropy/compositionally complex perovskites are yet to be characterised in detail. As a consequence of a large number of different compositions available from this approach, structural studies of the factors influencing their phase stability are essential to future work.

In order to understand the effects of different cations in these compositionally complex perovskites and their stabilising factors, a study of compositionally complex perovskites with lanthanides at the A-site and transition metals at the B-site is presented. The lanthanides oxides were used to determine the compositional flexibility over the A-site of the perovskite structure and were chosen from the larger Ln^{3+} cations from La to Dy. Ce, Pr and Tb were excluded due to their variable 3/4+ oxidation states. Substitutions with Ca and Sr to influence the charge balance at the B-site were also performed. The B-site cations were chosen from the 3d transition metals, which are known to form ABO_3 structures crystallising in *Pnma* or *R3̄c* at similar sintering temperatures, i.e. excluding Sc, V and Zn oxides. The compounds' structure and phase stability were studied by X-ray and neutron diffraction whilst chemical states were probed using X-ray photon electron spectroscopy (XPS), and

their magnetic properties were investigated using magnetometry.

The results of these investigations suggest that these compositions can be described as solid solutions stabilised by ionic size compatibility and charge balancing, and that the temperature of the structural transition from *Pnma* to *R3̄c* symmetry can be related to the pseudo cubic unit cell volume. The results form a guiding principle to the synthesis of oxides with 5 or more cations in equimolar or close to equimolar compositions simultaneously on the A and B-sites in the ABO_3 perovskite structure.

2. Experimental

Samples were prepared using traditional solid-state synthesis methods. Lanthanide oxides with purity >99.9% were pre-dried at 975 °C prior to weighing and mixed in stoichiometric proportions with the necessary metal oxides (TiO_2, Cr_2O_3, MnO, Fe_2O_3, Co_3O_4, NiO, CuO) with purity > 99.5%. For substitutions with Ca and Sr at the A-site, $CaCO_3$ and $SrCO_3$ with purity >99.9% were used. The mixtures were ground in ethanol and pressed into pellets before heating. The pellets were heated in air at 900 °C for 12 h, then at 1000 °C for 24 h and 1100 °C for 48 h with intermediate grindings. The heating and cooling rates were kept at 5 °C/min during sintering, and the cooling rate did not appear to affect the final product. Samples without CuO underwent an additional heating step at 1250 °C for 48 h. After sintering the densities were close to 85% of the theoretical density.

Powder X-ray diffraction (PXRD) patterns were collected at room temperature using a Bruker D8 ADVANCE diffractometer equipped with a Lynx-eye XE position sensitive detector (PSD) and Cu Kα radiation, and a Bruker D8 with a focusing Cu Kα1 monochromator and a Lynx-eye PSD. Diffraction patterns were collected within the range of 10–100° with a step size of 0.01°.

Structural changes as a function of temperature were investigated by synchrotron radiation powder X-ray diffraction using a custom-built sample cell [24] at the P02.1 beamline at PETRA III (λ = 0.207 Å) [25]. Samples were placed in single crystal sapphire capillaries and heated to 900 °C in an air atmosphere using a Kanthal wire coiled around the capillary, followed by rapid cooling. During the experiments, images of the scattered X-rays were recorded on a PerkinElmer XRD1621 fast area detector, and the resulting 2D images were azimuthally integrated to 1D diffraction patterns using the software Fit2D [26]. Instrument peak shape parameters and zero-point error were obtained from refinements based on data collected on LaB_6. The data were analysed by sequential Rietveld refinements as implemented in the software TOPAS [27,28].

Two sets of neutron powder diffraction data were collected, one using the MEREDIT instrument at the Nuclear Physics institute in Rez, Czech Republic and a second using the Polaris time of flight diffractometer at the ISIS pulsed spallation neutron source, Rutherford Appleton Laboratory, United Kingdom [29]. During measurements at the MEREDIT instrument, a copper mosaic monochromator (reflection 220) was used, giving a wavelength of 1.46 Å. Each pattern was collected in a 2θ-range of 4–144° at discrete temperatures ranging from 10 to 1200 K. The obtained powder diffraction patterns were analysed in sequence with the Rietveld method [30] implemented in the software FullProf [31]. For data collection on the Polaris diffractometer, approximately 3 g of powder was loaded into in a 6 mm diameter thin-walled vanadium sample can which was either mounted on an automatic sample changer for data collection at room temperature (293 K) or loaded into a helium flow "orange" cryostat (AS Scientific Products, Abingdon, UK) for data collection at 4 K [32]. Data reduction and generation of files suitable for profile refinement used the Mantid open source software [33]. Multi-histogram refinement using the software FullProf [31], where instrument specific parameters (e.g. background and parameters related to the full width at half maximum (FWHM)), as well as structural parameters (unit cell parameters, atomic positions, atomic displacement parameters (ADPs) and the occupancy for the oxygen ions) were allowed to refine. The ADPs were allowed to refine but constrained to have the same values for one
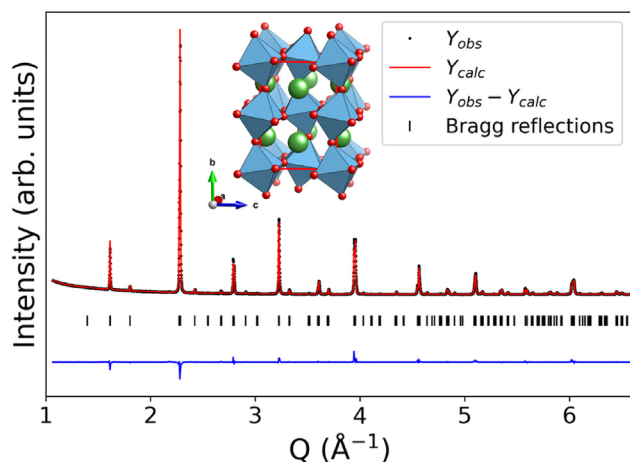
Fig. 1. Fitted room temperature powder X-ray diffraction data (CuKα₁) from LaM(7)O₃ after Rietveld structure refinement (R_{wp} = 5.84%) and structural model of the disordered perovskite with MO_6 octahedra in blue and A cations in green. (For interpretation of the references to colour in this figure legend, the reader is referred to the Web version of this article.)

crystallographic position (La/Nd and M(7) ions) and atomic type.

X-ray photoelectron spectroscopy (XPS) was conducted using an Ulvac-Phi Quantera II spectrometer with monochromatic Al Kα radiation (1486.7 eV). The analysis spot was set to a diameter of 100 μm, and an electron take-off angle of 45° was used. Measurements were conducted on sintered pellets of the samples under constant charge neutralisation with an electron flood gun and low energy Ar^+ ions. To remove adsorbed surface contaminants and minimise the effect of Ar^+ induced reduction of B-cation species, a pre-sputter step was employed using a 200 eV Ar^+ ion beam for 60 s. Survey and core-level spectra for all elements were collected. Adventitious carbon was used as charge reference and the position of the C 1s peak before sputtering was 284.8 eV.

The magnetisation measurements were performed using an MPMS SQUID magnetometer and PPMS Physical Properties Measurement System, both from Quantum Design Inc. The temperature dependence of magnetisation (M) was recorded under zero-field cooled (ZFC), and field cooled (FC) conditions under the application of a constant magnetic field H = 80 kA/m (1000 Oe). Magnetic hysteresis curves were recorded at a constant temperature T = 5 K, 10 K or 300 K with magnetic fields swept between ±4000 kA/m (±50 kOe; MPMS) or ± 7200 kA/m (±90 kOe; PPMS).

Powder morphology and composition were obtained using a ZEISS Leo 1550 field emission scanning electron microscope (SEM) equipped with an AZtec energy dispersive X-ray detector for spectroscopy analysis (EDS). Pellets of sintered powders were attached to a conducting carbon tape, and point EDS measurements were performed using 20 kV on at least 10 spots.

3. Results and discussion

The approach of mixing metal oxides with different solubilities while maintaining electroneutrality adopted by Rost et al. [17] has also been attempted in this study using binary oxides to form double perovskites with different solubilities. By doing that, samples with 7 elements at the B-site could be successfully synthesised within a single perovskite phase. Thereafter, substitutions on the A-site were applied, and thus, the complexity could be increased to include up to 13 cations in a single-phase perovskite material. By the process of chemical substitution, the question of which factors define phase stability can be investigated through observation of impurity phases and structural parameters. The results are presented first with a systematic crystallographic investigation at room temperature including the valence states from XPS and
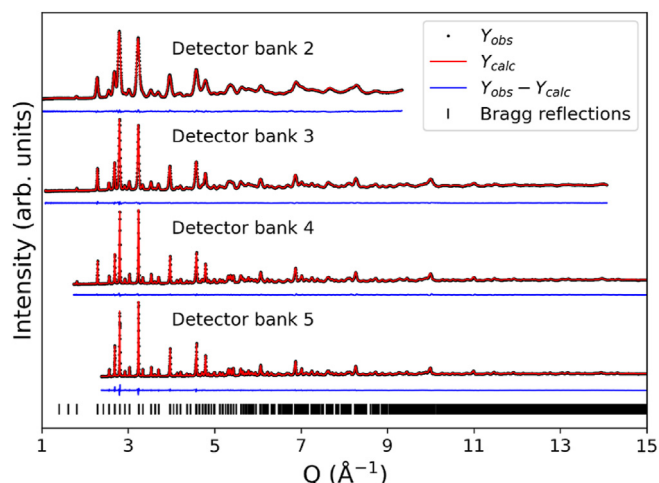

Fig. 2. Fitted room temperature powder neutron diffraction patterns from LaM(7)O₃ after multi-histogram Rietveld structure refinement. Total χ^2 = 4.26%, R_{Bragg} = 4.05, 4.23, 2.42 and 1.62% for Banks 5, 4, 3 and 2, respectively.

microstructure. Thereafter, the thermal stability is determined from *in-situ* diffraction and finally the magnetic behaviour is discussed. For simplicity, the chemical formulas are abbreviated in the text to LnM(n)O₃ where n is the number of cations in equimolar concentrations at the B-site.

3.1. $LaTi_{1/7}Cr_{1/7}Mn_{1/7}Fe_{1/7}Co_{1/7}Ni_{1/7}Cu_{1/7}O_3$ (LaM(7)O₃)

The stepwise sintering procedure allowed for monitoring of the reaction's progress using PXRD analysis. After the first sintering step at 900 °C for 12 h, lanthanum oxide, double perovskite phases, and several oxide phases were present. A second sintering at 1000 °C for 24 h resulted in a single perovskite phase with orthorhombic symmetry and a subsequent heat treatment at 1100 °C improved the crystallinity. The phase evolution of La₀.₅Nd₀.₅M(7)O₃ at the intermediate sintering temperatures is shown in Figure S1.

The X-ray diffraction pattern of the final product showed a single phase with no significant peak broadening. The pattern collected on LaM(7)O₃ was indexed in space group *Pnma* with a = 5.5255(1), b = 7.7829(1), c = 5.4980(1) Å and V = 236.4(1) Å³, as shown in Fig. 1 and Tables S1, S2. These are similar to those observed for *e.g.* LaCrO₃, a = 5.5147(6), b = 7.756(1), c = 5.4796(6) Å and V = 234.5(1) Å³.

The morphology and composition of the sample were investigated using SEM and EDS analysis. SEM images of the surface of a sintered pellet of LaM(7)O₃ revealed a porous surface with grain sizes < 2 μm (Figure S2), which suggests a slow grain coarsening process. The result of EDS point analysis of more than 10 spots indicated an average cation composition of La51.0(9)Ti7.4(4)Cr7.2(2)Mn7.5(6)Fe6.6(6)Co7.1(4)Ni7.1(2)Cu6.2(4) (excluding the oxygen content) and are close to the expected nominal composition of 7.1 at the B-site, for full results see Table S3 and Figures S3 and S4. The sample is slightly deficient in Cu, most likely as a result of the low melting point of CuO.

3.2. Room temperature structure from neutron powder diffraction

A sample with partial substitution on the A-site, but keeping the 7 elements on the B-site, giving La₁/₂Nd₁/₂M(7)O₃ was synthesised to study the atomic positions and occupancies of the constituting elements using neutron powder diffraction. The Nd substitution was chosen to increase the orthorhombic distortion and facilitate the refinements, but only partial substitution was implemented to avoid excessive neutron absorption. The fitted diffraction patterns from four out of the five detector banks from the Polaris instrument for the La₁/₂Nd₁/₂M(7)O₃ sample are visualised in Fig. 2. The refinement confirms the single phase

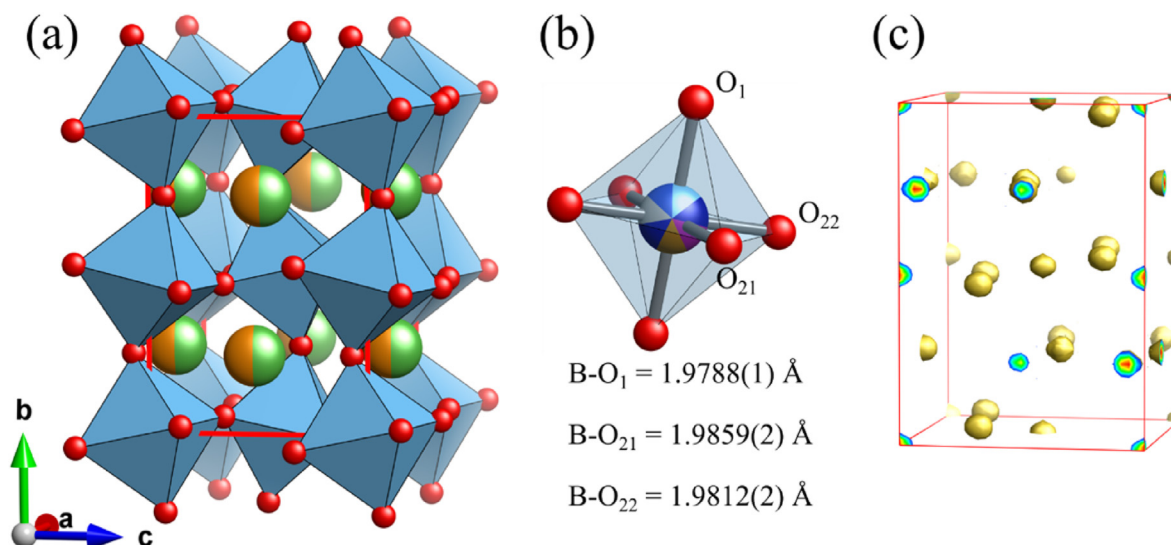**Fig. 3.** Structural model of $La_{1/2}Nd_{1/2}M(7)O_3$ showing (a) the oxygen positions, (b) transparent octahedra of the B-site with the calculated B cation to oxygen bond distances and (c) calculated nuclear density map (isosurface level set to 0.33 fm/Å^3).

Table 1
Refined atomic positions, occupancy (fixed to 1/2 for each lanthanide and 1/7 for each transition metal) and ADPs from NPD at room temperature for $La_{1/2}Nd_{1/2}M(7)O_3$ using the space group Pnma.

Ion	Wyckoff position	x	y	z	Occupancy	B_{iso}
Ln	4c	0.46495(2)	0.25	0.00766(5)	1	0.624(2)
M	4a	0	0	0	1	0.370(2)
O1	4c	0.51411(4)	0.25	0.57390(5)	1.0(1)	0.798(1)
O2	8d	0.21351(3)	0.03910(3)	0.28631(3)	1.0(1)	0.798(1)

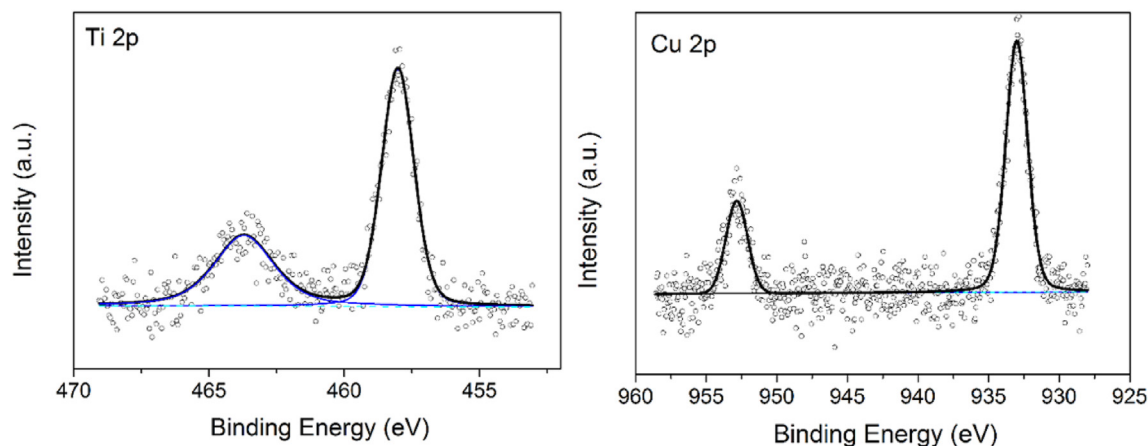**Fig. 4.** XPS spectra for Ti 2p and Cu 2p collected on a SmM(7)O$_3$ compound. Raw data is plotted with grey open circles and the results of peak fitting with lines (peak sum in black, individual peaks in blue and background in dashed blue). (For interpretation of the references to colour in this figure legend, the reader is referred to the Web version of this article.)

character for $La_{1/2}Nd_{1/2}M(7)O_3$, with the space group *Pnma* and $a = 5.5008(1)$, $b = 7.7419(2)$, $c = 5.4744(1)$ Å and $V = 233.1(1)$ Å^3. The occupancies were set to 1/2 each for La and Nd, and to 1/7 for each transition metal, however, refinements of the oxygen occupancies were allowed but did not vary from full occupancy. The unit cell is shown in Fig. 3a, where only a small distortion of the octahedra is observed, Fig. 3b. The calculated nuclear density map, Fig. 3c, especially shows that the oxygen position is well determined giving the shape of the oxygen spheres and no extra nuclear density in close proximity to the oxygen. Atomic positions and occupancies are summarised in Table 1.

3.3. Valence state determination

X-ray Photoelectron Spectroscopy (XPS) was used to investigate the transition metal oxidation states and, given that the La 3d$_{5/2}$ peaks overlap with the weak Ni 2p$_{3/2}$ peak at 853 eV, an analogous Sm based sample was synthesised with the nominal composition $Sm(Ti_{1/7}Cr_{1/7}Mn_{1/7}Fe_{1/7}Co_{1/7}Ni_{1/7}Cu_{1/7})O_3$. A detailed analysis and the spectra collected for all the elements in the SmM(7)O$_3$ sample are given in the SI. This analysis suggests that the oxidation states for the transition metal cations are $Ti^{4+}Cr^{3+}Mn^{3+/4+}Fe^{3+}Co^{3+}Ni^{3+}Cu^{1+}$ in this specific sample, with likely mixed oxidation states for Mn balancing the overall charge at

Table 2
Summary of the compounds investigated at room temperature.

Composition	Abbreviation	Space group	Unit cell parameters		
			a (Å)	b (Å)	c (Å)
LaTi$_{1/7}$Cr$_{1/7}$Mn$_{1/7}$Fe$_{1/7}$Co$_{1/7}$Ni$_{1/7}$Cu$_{1/7}$O$_3$	LaM(7)O$_3$	*Pnma*	5.5246(8)	7.778(1)	5.4984(8)
La$_{1/2}$Nd$_{1/2}$Ti$_{1/7}$Cr$_{1/7}$Mn$_{1/7}$Fe$_{1/7}$Co$_{1/7}$Ni$_{1/7}$Cu$_{1/7}$O$_3$	La$_{1/2}$Nd$_{1/2}$M(7)O$_3$	*Pnma*	5.5018(6)	7.7438(9)	5.4763(8)
SmTi$_{1/7}$Cr$_{1/7}$Mn$_{1/7}$Fe$_{1/7}$Co$_{1/7}$Ni$_{1/7}$Cu$_{1/7}$O$_3$	SmM(7)O$_3$	*Pnma*	5.549(1)	7.623(2)	5.366(2)
SmCr$_{1/5}$Mn$_{1/5}$Fe$_{1/5}$Co$_{1/5}$Ni$_{1/5}$O$_3$	SmM(5)O$_3$	*Pnma*	5.497(2)	7.612(3)	5.350(2)
LaCr$_{1/5}$Mn$_{1/5}$Fe$_{1/5}$Co$_{1/5}$Ni$_{1/5}$O$_3$	LaM(5)O$_3$	*Pnma*[a]	5.5074(8)	7.739(2)	5.4630(8)
LaTi$_{1/6}$Cr$_{1/6}$Mn$_{1/6}$Fe$_{1/6}$Co$_{1/6}$Ni$_{1/6}$O$_3$	LaM(7,-Cu)O$_3$	*Pnma*	5.5321(8)	7.806(1)	5.5225(8)
LaTi$_{1/8}$Cr$_{1/8}$Mn$_{2/8}$Fe$_{1/8}$Co$_{1/8}$Ni$_{1/8}$Cu$_{1/8}$O$_3$	LaM(7,+Mn)O$_3$	*Pnma*	5.527(1)	7.790(2)	5.503(1)
LaCr$_{1/7}$Mn$_{3/7}$Fe$_{1/7}$Co$_{1/7}$Ni$_{1/7}$O$_3$	LaM(5,+2Mn)O$_3$	*Pnma*	5.5239(9)	7.777(2)	5.4949(9)
LaTi$_{1/6}$Mn$_{1/6}$Co$_{2/6}$Ni$_{1/6}$Cu$_{1/6}$O$_3$	LaM(7,-Cr-Fe + Co)O$_3$	*Pnma*	5.509(1)	7.735(2)	5.4606(9)
La$_{0.8}$Ca$_{0.2}$Cr$_{1/5}$Mn$_{1/5}$Fe$_{1/5}$Co$_{1/5}$Ni$_{1/5}$O$_3$	La$_{0.8}$Ca$_{0.2}$M(5)O$_3$	*Pnma*	5.473(2)	7.691(4)	5.436(2)
La$_{0.8}$Sr$_{0.2}$Cr$_{1/5}$Mn$_{1/5}$Fe$_{1/5}$Co$_{1/5}$Ni$_{1/5}$O$_3$	La$_{0.8}$Sr$_{0.2}$M(5)O$_3$	$R\bar{3}c$	5.4813(5)	–	13.269(1)
LaTi$_{1/8}$Cr$_{1/8}$Mn$_{1/8}$Fe$_{1/8}$Co$_{2/8}$Ni$_{1/8}$Cu$_{1/8}$O$_3$	LaM(7,+Co)O$_3$	*Pnma*	7.750(2)	5.512(1)	5.4746(8)
LaTi$_{1/8}$Cr$_{1/8}$Mn$_{1/8}$Fe$_{2/8}$Co$_{1/8}$Ni$_{1/8}$Cu$_{1/8}$O$_3$	LaM(7,+Fe)O$_3$	*Pnma*	5.5282(5)	7.7869(9)	5.5055(7)

[a] A small amount of an $R\bar{3}c$ phase was observed but could not be indexed due to overlapping reflections with the *Pnma* phase.

the B-site to +3. Fig. 4 shows two of these spectra where the spectrum collected for the Ti 2p core level shows a sharp peak with a FWHM of 1.4 eV at 458.0 eV and no clear indication of oxidation states other than Ti^{4+} [34]. The observed binding energy for the Cu 2p$_{3/2}$ peak at 933.0 eV is only slightly higher than the literature value reported for Cu$_2$O of 932.5 eV [35] and the spectrum lacks. The spectrum lacks the satellite peaks that are observed in the spectrum of CuO [36]. Due to the preferred linear and planar coordinations for Cu$^+$ in oxides it cannot be ruled out that Cu will have mixed states in this perovskite structure that are not clearly detected with XPS analysis in these samples.

3.4. Phase purity with varying composition

The successful preparation of LaM(7)O$_3$ motivated a systematic investigation of the structural changes with increasing temperature and phase purity in samples with different cation compositions at both the A and B-sites. These syntheses include a substitution of the A-site cation,

various equimolar and non-equimolar compositions at the B-site and even with multiple atoms at both the A and B-sites. The compounds investigated in detail in this study are shown in Table 2, but for a list of all compounds synthesised see Table S4 in the supporting information (SI). The compounds presented in this study could be regarded as solid solutions of their binary oxides, as previously observed in LaM(5)O$_3$ [37]. Similarly, the average of the reduced unit cell volumes of the six simple SmBO$_3$ perovskites with B = Ti, Cr, Mn, Fe, Co, Ni (56.7 Å^3) is close to the values obtained for SmM(5)O$_3$ (56.0 Å^3) and SmM(7)O$_3$ (56.7 Å^3). For full details, see Tables S4, S5 and Figure S6 in SI. Substitution of the lanthanide with group II metals appears to be limited to a maximum x = 0.2 in La$_{1-x}$A$_x$M(5)O$_3$. These compositions have a charge of 2.8+ at the A-site and, without oxygen vacancies, a charge of 3.2+ at the B-site. The resulting charges of each B-site cations would be Cr^{3+} Mn^{4+} Fe^{3+} Co^{3+} Ni^{3+}, and further oxidation by increasing the x content is unfeasible. A selection of these compositions was chosen for further analysis to allow investigation of various aspects of the system. The effects of B-site composition were investigated by altering both the number of B-site cations and their concentration whilst the A-site substitution was probed through substitution with other lanthanides and group II metals.

3.5. Variable temperature in-situ diffraction

A detailed temperature dependent neutron powder diffraction investigation was performed up to 930 °C for the La$_{1/2}$Nd$_{1/2}$M(7)O$_3$ sample on the MEREDIT diffractometer in Rez. Pseudocubic unit cell parameters, phase fractions and bond distances for the B–O bonds are plotted in Fig. 5. The unit cell parameters increase continuously with increasing temperature until 700 °C, above which a second phase, having a trigonal $R\bar{3}c$ structure, coexists with the orthorhombic phase and small changes in the slopes of the a' and b' reduced unit cell parameters are observed. The absence of a group/subgroup relation between these space groups indicates the orthorhombic to trigonal phase transition is of first order. The structural model refinements show that there are no vacancies at the oxygen sites throughout the studied temperature interval and the M − O distances indicate no Jahn-Teller distortions of the octahedra at room temperature, although with increasing temperature, the equatorial distortion increases. This can be clearly observed as the B–O$_1$ distance follows the average M − O upon heating whereas the equatorial bond distances (B–O$_{21}$ and B–O$_{22}$) distorts in different directions compared to the average giving asymmetric M − O octahedra at elevated temperatures.

To study the structural phase transitions at high temperatures in several other compositionally complex perovskite samples, *in-situ* powder X-ray diffraction was performed between room temperature and 900 °C. As an example, the data for LaM(7)O$_3$ is shown in Fig. 6, where the *Pnma*-$R\bar{3}c$ transition occurs around 500 °C. The first set consists of LaM(7)O$_3$, LaM(7,-Cu)O$_3$ and LaM(5)O$_3$ with equimolar quantities of 7, 6 and 5 cations, respectively, on the B-site. It is worth noting that LaM(5)O$_3$ crystallises in a two-phase region already at room temperature, whereas previous reports suggest that the two-phase region for this composition exists only above 150 °C [38]. Furthermore, first-principles calculations have suggested a degeneracy of the orthorhombic and rhombohedral phases at room temperature for LaM(5)O$_3$ [37]. The second set of compositions consists of samples with 5 and 7 different cations but with non-equimolar concentrations of Mn and Co, which can display multiple oxidation states to balance the charge at the B-site. In the third set, the B-site cation content is fixed, whereas La^{3+} at the A-site was partially substituted with Ca^{2+} and Sr^{2+} in an attempt to increase the charges of the B cations and study the effect of A cation size on stability.

Perovskites with the composition LaMO$_3$ (M = first-row transition metal) predominantly crystallise in either orthorhombic *Pnma* or trigonal $R\bar{3}c$ space groups, where the latter symmetry is favoured by small B-site cations and high temperatures [39–45]. The two structures differ by their octahedral tilt system: the *Pnma* phase can be described through two
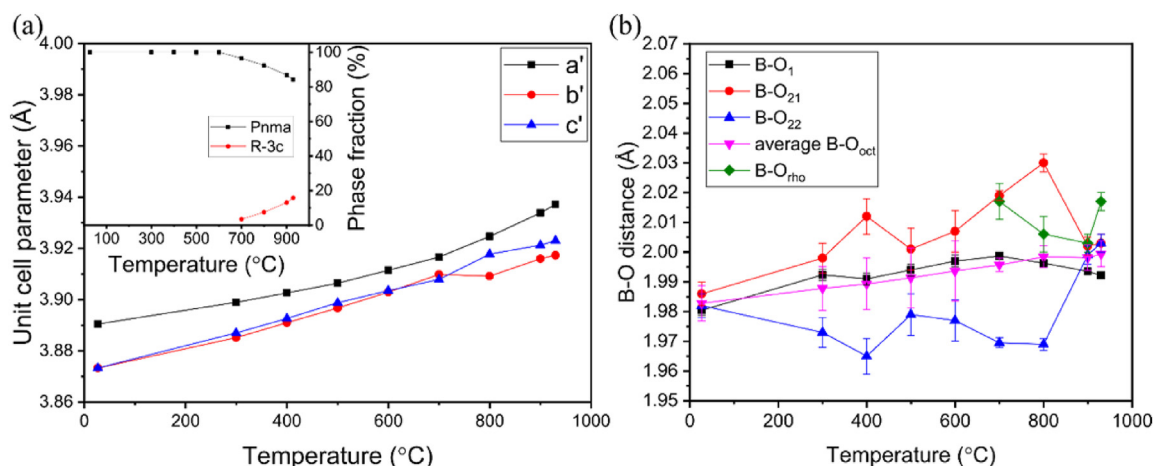
Fig. 5. The evolution of the $La_{1/2}Nd_{1/2}M(7)O_3$ perovskite sample from room temperature to 930 °C (a) the reduced unit cell parameters where $a' = \frac{a}{\sqrt{2}}$, $b' = \frac{b}{2}$, and $c' = \frac{c}{\sqrt{2}}$, and (b) the B cation to oxygen bond distance. Insert shows the phase content over the whole temperature span.
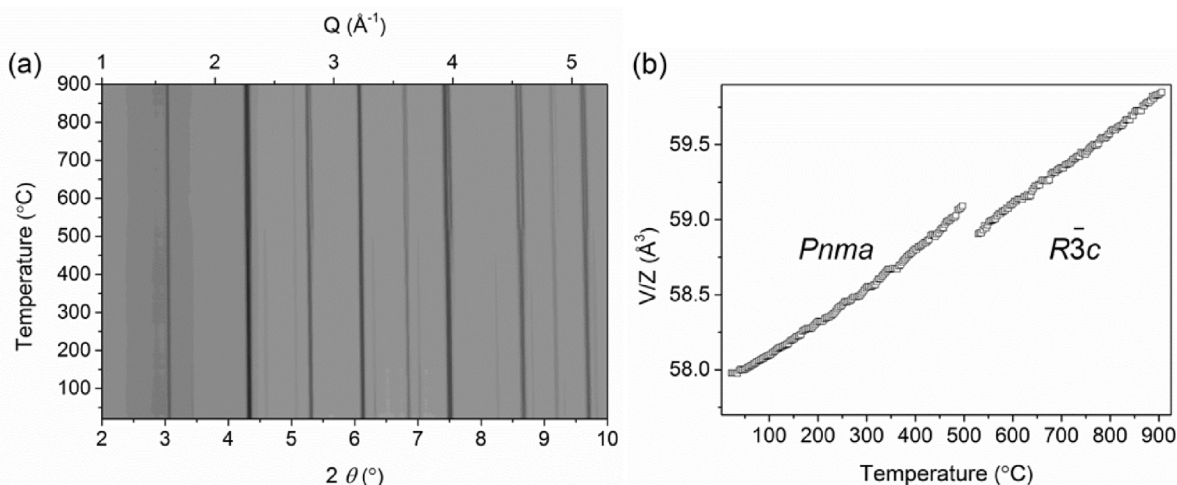

Fig. 6. (a) The diffraction patterns collected for $LaM(7)O_3$ with increasing temperature ($\lambda = 0.2071$ Å) and (b) V/Z as a function of temperature.

out-of-phase tilts of equal magnitude and an in-phase tilt along the third axis ($a^-a^-c^+$ in Glazer notation), whereas the $R\overline{3}c$ symmetry is driven by out-of-phase tilts polarised along all three axes of the pseudo-cube ($a^-a^-a^-$) [46,47]. The particular tilt system observed is dictated by the Goldschmidt tolerance factor and the optimization of the bonding environment for the A-site cation [20,48]. The compositionally complex perovskites presented in this work can be considered as multi-component solid solutions of the $LaMO_3$ systems and hence mirror their phase behaviour. The phase diagrams in Fig. 7 show that at low temperatures, *Pnma* symmetry is generally observed and increasing temperature leads to a first-order transition to the rhombohedral phase, with a region of coexisting phases. No evidence of B-site cation order was found for any of the systems under study, which would have reduced the symmetry to $P2_1/n$ and $R\overline{3}$, respectively [49]. The lack of B-site cation ordering was also confirmed with transmission electron microscopy and electron diffraction for the sample $Ln(6)M(7)O_3$ (full description in SI).

The observed temperature for the *Pnma*-$R\overline{3}c$ structural transition is highly dependent on the composition on both the A and B-sites. For example, as seen in Fig. 7, set 1 at the top, $LaM(5)O_3$ transitions to the $R\overline{3}c$ phase below 150 °C and a careful examination of the diffraction patterns reveals the presence of the two phases at room temperature, but the incorporation of Ti to give $LaM(6)O_3$ increases the transition temperature to above 750 °C. The further addition of Cu to produce the $LaM(7)O_3$ sample reduces the transition temperature to about 500 °C.

These observations can be correlated to the reduced cell volume at room temperature, V/Z being the largest for $LaM(7,-Cu)O_3$ and smallest for $LaM(5)O_3$. In the second set of samples shown in the third set, at the bottom of Fig. 7, the cation composition at the B-site is not equimolar; however, a similar trend with reduced unit cell volume is observed. In the Sr containing sample in Fig. 7, the A-site substitution with Sr^{2+} stabilises the rhombohedral phase across the entire temperature range studied due to the increased tolerance factor [48,50].

Within the compositionally complex perovskites studied with *in-situ* diffraction techniques, the phase transition between the Pnma and $R\overline{3}c$ space groups is seen to occur over a relatively large range of temperatures. Typically, the structures of perovskite-based materials can be predicted using the Goldschmidt tolerance factor as a guiding principle. However, this becomes more problematic given the nature of the compositionally complex perovskites studied here with uncertain/mixed oxidation and spin states of the B-site cations. Furthermore, approximate values of the tolerance factors could be determined based on oxidation states as determined from XPS data of $SmM(7)O_3$ (see section 3.3) and assuming low spin states [51]. The estimated tolerance factors fall within the expected range for the orthorhombic structure with values in the region of 0.96–0.99 but with very little variation upon B-site substitution and hence do not provide significant insight to their phase stability.

However, the reduced unit cell volumes do provide a trend to the structural stability of these systems. The relationship between the phase
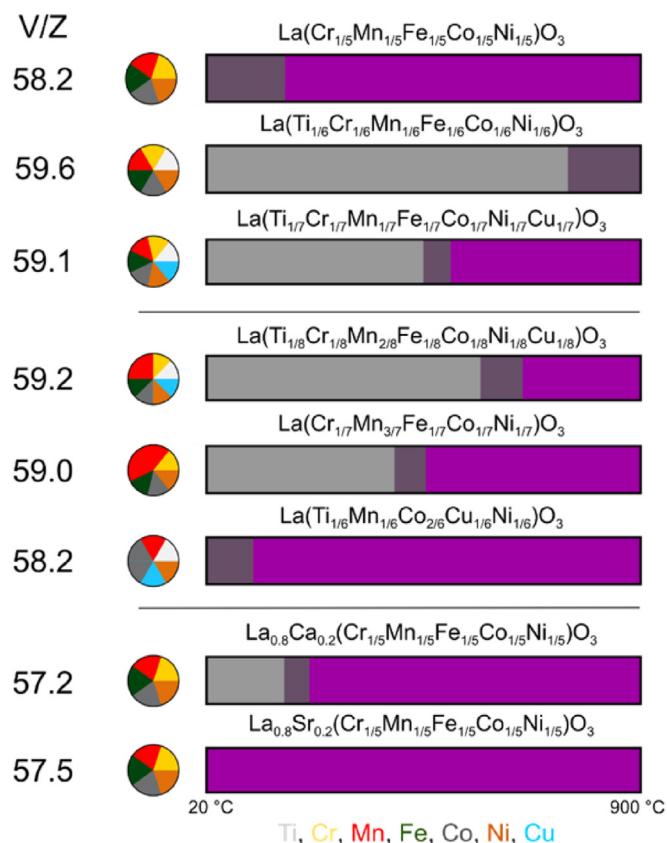
Fig. 7. Phase transitions of the studied samples as a function of temperature. Orthorhombic symmetry is denoted by grey, trigonal by purple and two-phase regions by dark grey. The relative atomic percent of each cation at the B-site is visualised by the coloured circle segments. The V/Z values are taken from room temperature refinements. (For interpretation of the references to colour in this figure legend, the reader is referred to the Web version of this article.)

transition temperature and the reduced unit cell volumes at room temperature is plotted in Fig. 8. A general trend is observed with larger unit cell volumes favouring higher phase transition temperatures, although there are some significant deviations to this relationship. Compounds with variations only in B-site composition (LaMO$_3$) obey this trend more strictly. However, in compositions with substitution of La at the A-site, the tolerance factor appears to be the dominant factor. In these cases, the

larger A-site radius favours the $R\bar{3}c$ crystal structure over the *Pnma* structure as previously reported in numerous compounds [40,41]. Whilst La$_{0.8}$Sr$_{0.2}$M(5)O$_3$ adopts $R\bar{3}c$ symmetry at room temperature, no phase transition temperature could be observed since the diffraction experiments were limited to 293–900 °C. At high temperature, the $R\bar{3}c$ crystal structure is expected to undergo a phase transition to a cubic space group, as observed in LaAlO$_3$ [52].

Phase purity can be achieved for both equimolar and non-equimolar samples over a range of compositions considering that no oxygen vacancies form and that the oxidation states of the B-site cations change accordingly to give charge neutrality. Despite their isostructural nature and little variation in tolerance factors, a very large degree of tunability in phase transition temperature can be achieved through subtle and small changes in the B-site composition. A similar effect has been reported in LaCrO$_3$, where the transition temperature is lowered by partial substitutions at the B-site with smaller cations as in La(Co,Cr)O$_3$ [53] or by substitutions at the A-site that increase the tolerance factor [54]. The clear correlation between reduced unit cell volume and phase transition temperature can thus be used to approximate the compounds' phase transition temperatures from room temperature cell parameters.

3.6. Magnetism

Given the large proportion of magnetic ions in the compositionally complex perovskites, the magnetic behaviour was investigated for La$_{1/2}$Nd$_{1/2}$M(7)O$_3$, LaM(7,+Mn)O$_3$, LaM(7,+Co)O$_3$, LaM(7,+Fe)O$_3$, LaM(5,+2Mn)O$_3$ and La$_{0.8}$Sr$_{0.2}$M(5)O$_3$. The temperature dependence of the magnetisation $M(T)$ is presented in Fig. 9. Magnetic hysteresis $M(H)$ curves recorded at T = 5 K are added as insets; 1 A m^2/kg represents ~0.043 μ_B/B-site for all samples. At 300 K all the samples exhibit linear paramagnetic-like $M(H)$ curves. The samples display different magnetic behaviour reflecting how the magnetic interaction is altered by the B-site cations and their respective concentrations. La$_{1/2}$Nd$_{1/2}$M(7)O$_3$ (Fig. 9a) shows a shape of the magnetisation and the inverse susceptibility curves that are reminiscent of a ferrimagnetic behaviour at low temperatures [55,56], or an antiferromagnetic (AFM) behaviour with a weak excess moment, smaller than 0.1 μ_B/f. u (see SI for details). This behaviour is consistent with earlier findings of magnetic compositionally complex perovskite samples [56]. The $M(T)$ curves of LaM(7,+Mn)O$_3$, LaM(7,+Co)O$_3$ and LaM(7,+Fe)O$_3$ are shown in Fig. 9b. All these samples exhibit a ferrimagnetic-like response akin to that observed for La$_{1/2}$Nd$_{1/2}$M(7)O$_3$. The temperature onset of ferrimagnetism is different for the four samples, about 180 K, 130 K, 100 K and 80 K for LaM(7,+Fe)O$_3$, LaM(7,+Mn)O$_3$, La$_{1/2}$Nd$_{1/2}$M(7)O$_3$ and LaM(7,+Co)O$_3$, respectively.
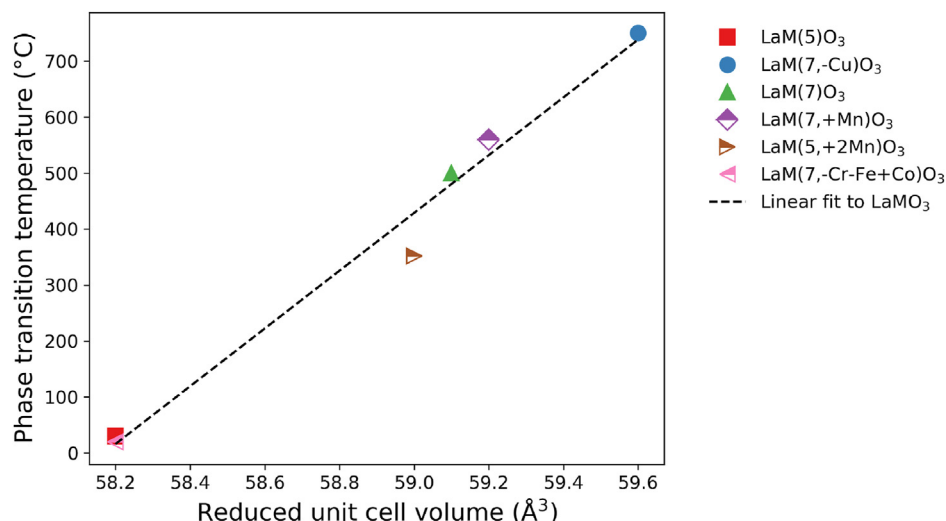

Fig. 8. Reduced unit cell volume vs phase transition temperature determined by in-situ X-ray diffraction for six of the compounds studied.
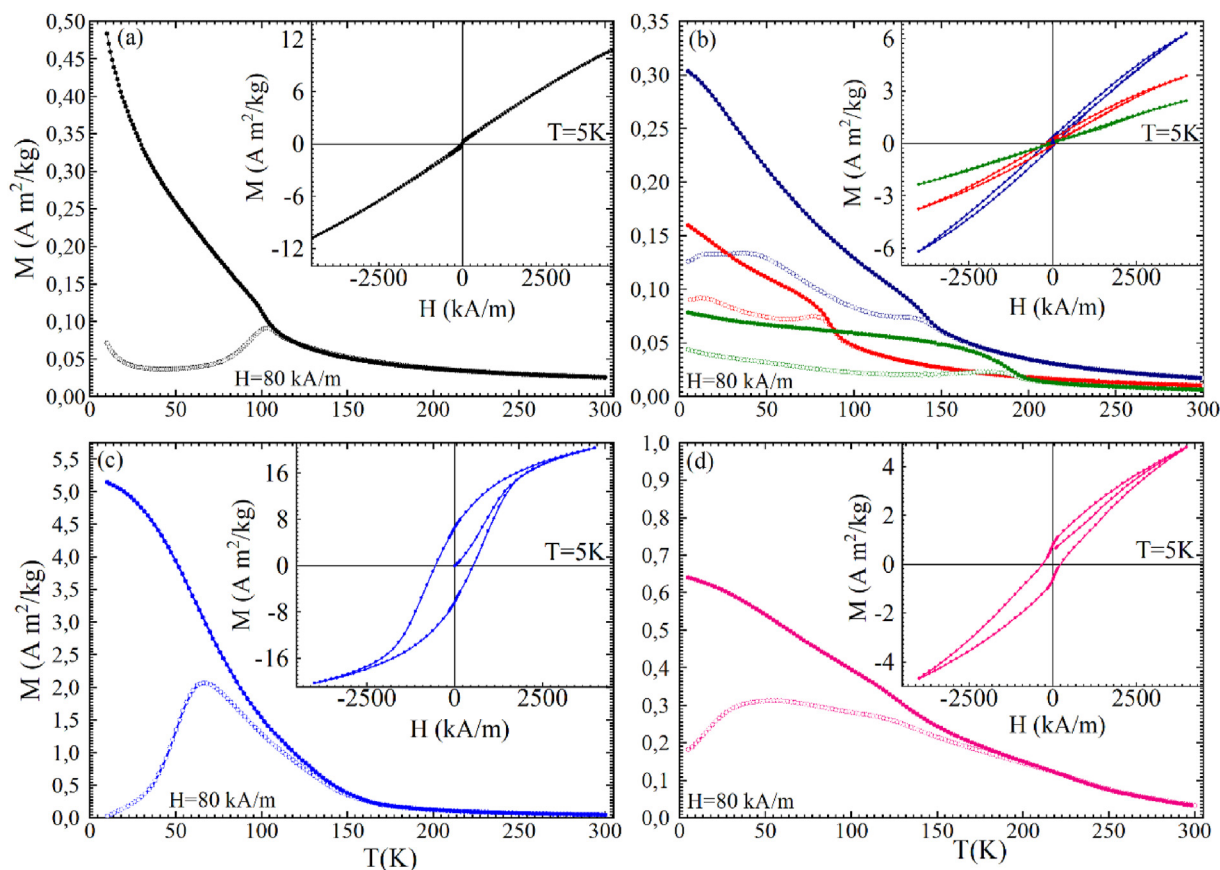
Fig. 9. Temperature dependence of magnetisation M(T) for (a) $La_{1/2}Nd_{1/2}Me(7)O_3$, (b) LaM(7,+Mn)O_3 (blue color), LaM(7,+Co)O_3 (red) and LaM(7,+Fe)O_3 (green), (c) LaM(5,+2Mn)O_3 and (d) $La_{0.8}Sr_{0.2}M(5)O_3$ under zero-field cooled and field cooled conditions; H = 80 kA/m (1000 Oe). Insets show the field dependence of the magnetisation M(H) measured at a constant temperature T = 5 K for the respective samples. (For interpretation of the references to colour in this figure legend, the reader is referred to the Web version of this article.)
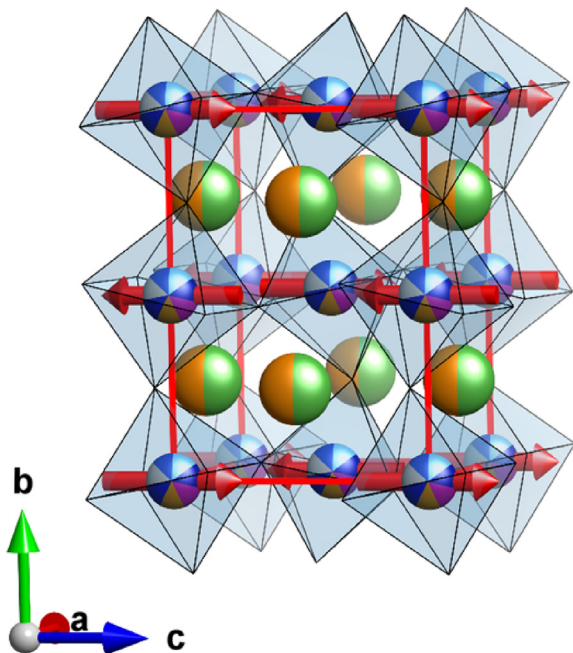

Fig. 10. Refined magnetic structure model of $La_{1/2}Nd_{1/2}M(7)O_3$, in the space group Pn'ma' at 4 K, giving a total magnetic moment of ~0.3 μB per B-site.

The high-field magnetisation values also differ (insets in Fig. 9a and b) while LaM(5,+2Mn)O_3 (Fig. 9c) displays a larger magnetisation and a large coercivity H_C ($M(T = 5$ K, H = 4000 kA/m) ~20 A m^2/kg and H_C ~470 kA/m (5875 Oe)). However, no clear transition is observed, in spite of a faint ferrimagnetic like inflection near 170 K. The temperature-dependent magnetisation curves suggest short-range magnetic order for LaM(5,+2Mn)O_3. The situation is similar for $La_{0.8}Sr_{0.2}M(5)O_3$ (Fig. 9d), where magnetic irreversibility is observed below ~250 K. There are several broad features in the $M(T)$ curves, and the $M(H)$ curves are more complex, suggesting a greater magnetic inhomogeneity in that system.

Given the complex magnetic behaviour of the compositionally complex perovskite samples, neutron powder diffraction data were collected from $La_{1/2}Nd_{1/2}M(7)O_3$ at 4K on the Polaris diffractometer at ISIS to investigate its magnetic structure. For a discussion of possible magnetic space groups (MSGs), the reader is referred to the SI. The best magnetic structure model that both fitted the NPD patterns and the magnetisation data, was found within the MSG *Pn'ma'*, Fig. 10. The structure is antiferromagnetic with magnetic moments only on the B-site with a total value of 0.32(4) μB along the x-direction. This magnetic structure model is compatible with the magnetometry results which suggested an AFM configuration with a weak excess moment.

4. Conclusions

The compositionally complex perovskite $LaTi_{1/7}Cr_{1/7}Mn_{1/7}Fe_{1/7}Co_{1/7}Ni_{1/7}Cu_{1/7}O_3$ (LaM(7)O_3) was synthesised through traditional solid-

state synthesis and analysed by X-ray diffraction, and SEM analysis. The diffraction data confirm a single-phase perovskite with *Pnma* symmetry and no evidence of cation ordering. The nominal composition of the compound was also confirmed by EDS analysis whilst the XPS analysis of the isostructural compound $SmTi_{1/7}Cr_{1/7}Mn_{1/7}Fe_{1/7}Co_{1/7}Ni_{1/7}Cu_{1/7}O_3$ revealed an unusual Cu^+ oxidation state and suggested mixed oxidation states of $Mn^{3/4+}$.

Room temperature neutron diffraction data of the related $La_{1/2}Nd_{1/2}M(7)O_3$ revealed a crystal structure isostructural to $LaM(7)O_3$ with no evidence of oxygen vacancies. The effects of composition on both the structure and phase stability were investigated with variable-temperature synchrotron PXRD. This revealed a phase transition between the *Pnma* and *R$\overline{3}$c* space groups with a large degree of tunability of the transition temperature with composition. The phase transition temperature has a dependence on the reduced unit cell volumes rather than solely on the Goldschmidt tolerance factor.

The effects of composition upon the magnetic properties were also investigated, and magnetometry of selected samples revealed a low-temperature ferrimagnetic phase transition. Both the phase transition temperature and magnetisation display a strong dependence with respect to composition. The magnetic structure was determined from low temperature neutron diffraction data of $La_{1/2}Nd_{1/2}M(7)O_3$ which revealed magnetic ordering below 100 K and an antiferromagnetic structure described by the magnetic space group *Pn'ma'*.

The perovskites presented in this work suggests that this range of compositions can be considered to be solid solutions stabilised by compatible ionic sizes and charge balancing. Compositionally complex compositions provide the opportunity for fine tuning physical properties and structural transitions, which could be applied to other perovskites and oxides. It is expected that the findings presented in this will lead to the design of new compositions with interesting thermoelectric, magnetic and transport properties. Furthermore, it is likely that many of these properties will exhibit large tunability given the large number of possible cation and anion combinations in these complex perovskites.

CRediT authorship contribution statement

Johan Cedervall: Investigation, Writing – original draft, Writing – review & editing, Visualization. **Rebecca Clulow:** Investigation, Writing – original draft, Writing – review & editing, Visualization. **Hanna L.B. Boström:** Investigation, Writing – original draft, Visualization. **Deep C. Joshi:** Investigation, Writing – original draft, Visualization. **Mikael S. Andersson:** Investigation. **Roland Mathieu:** Investigation, Writing – original draft. **Premysl Beran:** Investigation. **Ronald I. Smith:** Investigation. **Jo-Chi Tseng:** Investigation. **Martin Sahlberg:** Supervision, Funding acquisition, Project administration. **Pedro Berastegui:** Investigation, Writing – original draft, Visualization. **Samrand Shafeie:** Investigation, Writing – original draft, Visualization.

Declaration of competing interest

The authors declare that they have no known competing financial interests or personal relationships that could have appeared to influence the work reported in this paper.

Appendix A. Supplementary data

Supplementary data to this article can be found online at https://doi.org/10.1016/j.jssc.2021.122213.

References

[1] M.M. Vijatović, J.D. Bobić, B.D. Stojanović, History and challenges of barium titanate: Part I, Sci. Sinter. 40 (2008) 155–165.
[2] A. Chroneos, R.V. Vovk, I.L. Goulatis, L.I. Goulatis, Oxygen transport in perovskite and related oxides: a brief review, J. Alloys Compd. 494 (2010) 190–195.
[3] M.L. Medarde, Structural, magnetic and electronic properties of RNiO₃ perovskites (R = rare earth), J. Phys. Condens. Matter 9 (1997) 1679–1707.
[4] Ronald E. Cohen, Origin of ferroelectricity in perovskite oxides, Nature 358 (1992) 136–138.
[5] J. Mitchell, D. Argyriou, C. Potter, D. Hinks, J. Jorgensen, S. Bader, Structural phase diagram of La_{1−x}Sr_{x}MnO_{3+δ}: relationship to magnetic and transport properties, Phys. Rev. B 54 (1996) 6172–6183.
[6] A. Mellergård, R.L. McGreevy, S.G. Eriksson, Structural and magnetic disorder in La₁₋ₓ SrₓMnO₃, J. Phys. Condens. Matter 12 (2000) 4975–4991.
[7] C.N.R. Rao, Charge, spin, and orbital ordering in the perovskite manganates, Ln₁₋ₓAₓMnO₃ (Ln = Rare Earth, a = Ca or Sr), J. Phys. Chem. B 104 (2000) 5877–5889.
[8] J. Cohn, J. Neumeier, C.P. Popoviciu, K.J. McClellan, T. Leventouri, Local lattice distortions and thermal transport in perovskite manganites, Phys. Rev. B 56 (1997) R8495–R8498.
[9] A.A. Bokov, Z.G. Ye, Recent progress in relaxor ferroelectrics with perovskite structure, J. Mater. Sci. 41 (2006) 31–52.
[10] M. Paciak, T.R. Welberry, J. Kulda, M. Kempa, J. Hlinka, Polar nanoregions and diffuse scattering in the relaxor ferroelectric PbMg₁/₃Nb₂/₃O₃, Phys. Rev. B 85 (2012) 1–9.
[11] P.D. Battle, S.I. Evers, E.C. Hunter, M. Westwood, La₃Ni₂SbO₉: a relaxor ferromagnet, Inorg. Chem. 52 (2013) 6648–6653.
[12] V.V. Lemanov, E.P. Smirnova, N.V. Zaĭtseva, Relaxors with multiple substitutions in octahedral sites of the perovskite structure, Phys. Solid State 51 (2009) 1685–1690.
[13] Y. Sharma, B.L. Musico, X. Gao, C. Hua, A.F. May, A. Herklotz, A. Rastogi, D. Mandrus, J. Yan, H.N. Lee, M.F. Chisholm, V. Keppens, T.Z. Ward, Single-crystal high entropy perovskite oxide epitaxial films, Phys. Rev. Mater. 2 (2018) 1–6.
[14] S. Jiang, T. Hu, J. Gild, N. Zhou, J. Nie, M. Qin, T. Harrington, K. Vecchio, J. Luo, A new class of high-entropy perovskite oxides, Scripta Mater. 142 (2018) 116–120.
[15] J. Gild, Y. Zhang, T. Harrington, S. Jiang, T. Hu, M.C. Quinn, W.M. Mellor, N. Zhou, K. Vecchio, J. Luo, High-entropy metal diborides: a new class of high-entropy materials and a new type of ultrahigh temperature ceramics, Sci. Rep. 6 (2016) 1–10.
[16] E. Castle, T. Csanádi, S. Grasso, J. Dusza, M. Reece, Processing and properties of high-entropy ultra-high temperature ceramic carbides, Sci. Rep. 8 (2018) 1–12.
[17] C.M. Rost, E. Sachet, T. Borman, A. Moballegh, E.C. Dickey, D. Hou, J.L. Jones, S. Curtarolo, J.P. Maria, Entropy-stabilized oxides, Nat. Commun. 6 (2015) 1–8.
[18] D. Berardan, A.K. Meena, S. Franger, C. Herrero, N. Dragoe, Controlled Jahn-Teller distortion in (MgCoNiCuZn)O-based high entropy oxides, J. Alloys Compd. 704 (2017) 693–700.
[19] A.J. Wright, J. Luo, A step forward from high-entropy ceramics to compositionally complex ceramics: a new perspective, J. Mater. Sci. 55 (2020) 9812–9827.
[20] V.M. Goldschmidt, Die Gesetze der Krystallochemie, Naturwissenschaften 14 (1926) 477–485.
[21] P.B. Meisenheimer, J.T. Heron, Oxides and the high entropy regime: a new mix for engineering physical properties, MRS Adv 5 (2020) 3419–3436.
[22] R.Z. Zhang, M.J. Reece, Review of high entropy ceramics: design, synthesis, structure and properties, J. Mater. Chem. A. 7 (2019) 22148–22162.
[23] C. Oses, C. Toher, S. Curtarolo, High-entropy ceramics, Nat. Rev. Mater. 5 (2020) 295–309.
[24] T.R. Jensen, T.K. Nielsen, Y. Filinchuk, J.E. Jrgensen, Y. Cerenius, E.M.A. Gray, C.J. Webb, Versatile in situ powder X-ray diffraction cell for solid-gas investigations, J. Appl. Crystallogr. 43 (2010) 1456–1463.
[25] A.C. Dippel, H.P. Liermann, J.T. Delitz, P. Walter, H. Schulte-Schrepping, O.H. Seeck, H. Franz, Beamline P02.1 at PETRA III for high-resolution and high-energy powder diffraction, J. Synchrotron Radiat. 22 (2015) 675–687.
[26] A.P. Hammersley, S.O. Svensson, M. Hanfland, A.N. Fitch, D. Hausermann, Two-dimensional detector software: from real detector to idealised image or two-theta scan, High Pres. Res. 14 (1996) 235–248.
[27] H.M. Rietveld, Line profiles of neutron powder-diffraction peaks for structure refinement, Acta Crystallogr. 22 (1967) 151–152.
[28] A.A. Coelho, Topas-Academic.
[29] R.I. Smith, S. Hull, M.G. Tucker, H.Y. Playford, D.J. McPhail, S.P. Waller, S.T. Norberg, The upgraded Polaris powder diffractometer at the ISIS neutron source, Rev. Sci. Instrum. 90 (2019).

[30] H.M. Rietveld, A profile refinement method for nuclear and magnetic structures, J. Appl. Crystallogr. 2 (1969) 65–71.

[31] J. Rodríguez-Carvajal, Recent advances in magnetic structure determination by neutron powder diffraction, Phys. B Phys. 192 (1993) 55–69.

[32] ISIS Data RB1990322-1 http://doi.org/10.5286/ISIS.E.RB1990322-1, (n.d.).

[33] O. Arnold, J.C. Bilheux, J.M. Borreguero, A. Buts, S.I. Campbell, L. Chapon, M. Doucet, N. Draper, R. Ferraz Leal, M.A. Gigg, V.E. Lynch, A. Markvardsen, D.J. Mikkelson, R.L. Mikkelson, R. Miller, K. Palmen, P. Parker, G. Passos, T.G. Perring, P.F. Peterson, S. Ren, M.A. Reuter, A.T. Savici, J.W. Taylor, R.J. Taylor, R. Tolchenov, W. Zhou, J. Zikovsky, Mantid - data analysis and visualization package for neutron scattering and μ SR experiments, Nucl. Instruments Methods Phys. Res. Sect. A Accel. Spectrometers, Detect. Assoc. Equip. 764 (2014) 156–166.

[34] U. Diebold, T.E. Madey, TiO_2 by XPS, Surf. Sci. Spectra 4 (1996) 227–231.

[35] R.P. Vasquez, Cu_2O by XPS, Surf. Sci. Spectra 5 (1998) 257–261.

[36] R.P. Vasquez, CuO by XPS, Surf. Sci. Spectra 5 (1998) 262–266.

[37] M. Brahlek, A.R. Mazza, K.C. Pitike, E. Skoropata, J. Lapano, G. Eres, V.R. Cooper, T.Z. Ward, Unexpected crystalline homogeneity from the disordered bond network in $La(Cr_{0.2} Mn_{0.2}Fe_{0.2}Co_{0.2}Ni_{0.2})$ O_3 films, Phys. Rev. Mater. 4 (2020) 1–9.

[38] A. Sarkar, R. Djenadic, D. Wang, C. Hein, R. Kautenburger, O. Clemens, H. Hahn, Rare earth and transition metal based entropy stabilised perovskite type oxides, J. Eur. Ceram. Soc. 38 (2018) 2318–2327.

[39] D.B. Currie, M.T. Weller, Structure of $LaCuO_3$ by powder neutron diffraction, Acta Crystallogr. Sect. C Cryst. Struct. Commun. 47 (1991) 696–698.

[40] J.L. García-Muñoz, J. Rodríguez-Carvajal, P. Lacorre, J.B. Torrance, Neutron-diffraction study of $RNiO_3$ (R=La,Pr,Nd,Sm): electronically induced structural changes across the metal-insulator transition, Phys. Rev. B 46 (1992) 4414–4425.

[41] A.C. Komarek, H. Roth, M. Cwik, W.D. Stein, J. Baier, M. Kriener, F. Bourée, T. Lorenz, M. Braden, Magnetoelastic coupling in $RTiO_3$ (R=La,Nd,Sm,Gd,Y) investigated with diffraction techniques and thermal expansion measurements, Phys. Rev. B 75 (2007) 1–12.

[42] K. Oikawa, T. Kamiyama, T. Hashimoto, Y. Shimojyo, Y. Morii, Structural phase transition of orthorhombic $LaCrO_3$ studied by neutron powder diffraction, J. Solid State Chem. 154 (2000) 524–529.

[43] J. Rodríguez-Carvajal, M. Hennion, F. Moussa, A. Moudden, L. Pinsard, A. Revcolevschi, Neutron-diffraction study of the Jahn-Teller transition in stoichiometric, Phys. Rev. B 57 (1998) R3189–R3192.

[44] S.M. Selbach, J.R. Tolchard, A. Fossdal, T. Grande, Non-linear thermal evolution of the crystal structure and phase transitions of $LaFeO_3$ investigated by high temperature X-ray diffraction, J. Solid State Chem. 196 (2012) 249–254.

[45] G. Thornton, B.C. Tofield, A.W. Hewat, A neutron diffraction study of $LaCoO_3$ in the temperature range 4.2 < T < 1248 K, J. Solid State Chem. 61 (1986) 301–307.

[46] A.M. Glazer, The classification of tilted octahedra in perovskites, Acta Crystallogr. B 28 (1972) 3384–3392.

[47] C.J. Howard, H.T. Stokes, Group-theoretical analysis of octahedral tilting in perovskites. Erratum, Acta Crystallogr. Sect. B Struct. Sci. 58 (2002), 565–565.

[48] P.M. Woodward, Octahedral tilting in perovskites. II. Structure stabilizing forces, Acta Crystallogr. Sect. B Struct. Sci. 53 (1997) 44–66.

[49] C.J. Howard, B.J. Kennedy, P.M. Woodward, Ordered double perovskites - a group-theoretical analysis, Acta Crystallogr. Sect. B Struct. Sci. 59 (2003) 463–471.

[50] G. King, P.M. Woodward, Cation ordering in perovskites, J. Mater. Chem. 20 (2010) 5785–5796.

[51] R.D. Shannon, Revised effective ionic radii and systematic studies of interatomic distances in halides and chalcogenides, Acta Crystallogr. A 32 (1976) 751–767.

[52] H. Lehnert, H. Boysen, J. Schneider, F. Frey, D. Hohlwein, P. Radaelli, H. Ehrenberg, A powder diffraction study of the phase transition in $LaAlO_3$, Zeitschrift Fur Krist 215 (2000) 536.

[53] B. Gilbu, H. Fjellvåg, A. Kjekshus, J. Springborg, D.-N. Wang, G.B. Paulsen, R.I. Nielsen, C.E. Olsen, C. Pedersen, C.E. Stidsen, Properties of $LaCo_{(1-t)}Cr_{(t)}O_3$. I. Solid solubility, thermal expansion and structural transition, Acta Chem. Scand. 48 (1994) 37–45.

[54] K. Omoto, S.T. Norberg, S. Hull, A. Aoto, T. Hashimoto, Neutron diffraction study of the crystal structure and structural phase transition of $La_{0.7}Ca_{0.3-x}Sr_xCrO_3$ ($0 \leq x \leq$ 0.3). The relationship between thermodynamic behavior and crystal structure changes at the phase transition, J. Solid State Chem. 183 (2010) 392–401.

[55] P.L.C. Filho, P. Barrozo, D.A. Landinez-Tellez, R.F. Jardim, W.M. Azevedo, J. Albino Aguiar, Structural and magnetic properties of Ln_2CoMnO_6 (Ln = Dy and La) produced by combustion synthesis, J. Supercond. Nov. Magnetism 26 (2013) 2521–2524.

[56] R. Witte, A. Sarkar, R. Kruk, B. Eggert, R.A. Brand, H. Wende, H. Hahn, High-entropy oxides: an emerging prospect for magnetic rare-earth transition metal perovskites, Phys. Rev. Mater. 3 (2019) 1–8.